RSC Advances

PAPER

View Article Online
View Journal | View Issue

Cite this: *RSC Adv.*, 2025, **15**, 17130

Synergetic interplay of a nitrogen- and sulfur-rich copper bi-linker 2D cubic-layered MOF composite with MXene for improved hybrid supercapacitor application†

Maham Saeed,[a] Shahzad Sharif, *[a] Javed Hussain Shah,[a] Tayyaba Tur Rehman Afzal,[a] Muhammad Shahbaz,[a] Azhar Mehmood Shehzad,[a] Ayesha Shahzad,[a] Onur Şahin[b] and Sundas Shahzad[a]

To combine the properties of batteries and capacitors in a single hybrid device, metal–organic frameworks have emerged as promising materials. In this study, by incorporation of a heteroatom (N, O and S)-based bi-linker, a novel copper-based two-dimensional metal–organic framework (Cu-SIP-MOF), derived from 5-sulfoisophathalic acid monosodium salt (SIP sodium salt) and 4,4-bipyridine was synthesized and characterized using different techniques. The conductivity of the extended 2D MOF was attributed to π-d orbital contribution, which was further enhanced by fabricating its composite with MXene. The synthesized MOFs and its composites were electrochemically evaluated using different electroanalytical techniques such as cyclic voltammetry, galvanostatic charge–discharge and electrochemical impedance spectroscopy *via* three-electrode assembly. The composites of Cu-SIP-MOF with MXene (CM-200) in a 1 : 2 ratio possessed the highest specific capacity of 683.69 C g^{-1}, highlighting the potential for their practical implementation in asymmetric hybrid devices. The material demonstrated an energy density and a power density of 62 W h kg^{-1} and 2330.4 W kg^{-1}, respectively. It also expressed 98.3% coulombic efficiency after 5000 galvanic charge–discharge cycles. The significant values of specific capacity, energy density and power density of CM-200 make it a promising electrode material for a futuristic hybrid device.

Received 24th March 2025
Accepted 4th May 2025

DOI: 10.1039/d5ra02060c

rsc.li/rsc-advances

1. Introduction

To cater to the growing demand for stable energy sources, scientists are seeking to design potent and advanced energy storage devices.[1–4] Nowadays, batteries and supercapacitors are frequently used in various electronic devices, such as smartphones, laptops and home appliances.[5–7] Owing to the huge number of faradaic reactions occurring at the electrode, batteries show greater energy density; however, the extraction of high power density from them remains a challenging task so far.[8–10] In contrast, electrochemical capacitors exhibit superior cyclability and power density but have limited energy density compared to traditional batteries.[11–13] Hence, there is a dire need to design a system that exhibits the characteristics of both batteries and supercapacitors. A hybrid supercapacitor has one electrode with pseudocapacitive nature, responsible for high energy density, and the other electrode possesses capacitive nature with long duration cyclability.[14,15] For efficient electrochemical energy storage devices, the quality of the electrode materials should be very promising. The higher capacitance of the electric double-layer capacitor (EDLC) is due to charge separation between the electrolyte and electrode interface.[16] Many materials such as metal sulfides, oxides and phosphides are considered good for pseudocapacitive and battery-grade electrode materials. However, the development of new porous materials with rich electrochemical properties is a prerequisite to meet the requirements of advanced storage devices.[17]

The intrinsic characteristics of metal–organic frameworks (MOFs), such as shape, porous structure, greater surface area and durability, can help in customizing the structure of electrode materials to optimize electrochemical performance.[18–21] The highly porous structure of MOFs can be shaped by combining specific ratios of different metals and organic linkers.[18] Moreover, the presence of conjugation in the linkers constituting MOFs assists in electron transfer, while the rich porosity facilitates ion diffusion to promote redox reactions at the redox-active metal sites, resulting in improved

[a]*Materials Chemistry Laboratory, Institute of Chemical Sciences, Government College University Lahore, 54000, Pakistan. E-mail: mssharif@gcu.edu.pk*

[b]*Department of Occupational Health & Safety, Faculty of Health Sciences, Sinop University, TR-57000, Sinop, Turkey*

† Electronic supplementary information (ESI) available. CCDC 2311394. For ESI and crystallographic data in CIF or other electronic format see DOI: https://doi.org/10.1039/d5ra02060c

electrochemical performance of supercapacitors. However, the high stability and conductivity of MOFs have remained a challenging task for researchers.

Hydrogen bonding occurs in MOFs because of the presence of hydrophilic centers in organic ligands and metals. Various functional groups have been employed to enhance the structural stability of MOFs. The sulfonic acid ligand possesses two hydroxyl groups that can coordinate with the metal and have multiple sites to form a stable chelate structure.[22,23] Moreover, the presence of hetero atoms (N, O, S) in the aromatic linkers plays a vital role in the enhancement of surface properties like wettability for the efficient faradaic reactions with electrolyte ions. Because of lone pair electrons, they can cause extended pi-conjugation for better overlap of orbitals and can also donate electrons to metal nodes, thus increasing charge transportation and conductivity. Moreover, heteroatom-based linkers maintain structural stability after long cyclability, thereby sustaining their remarkable electrochemical performance.[24–26] Pyridine 2, 4, 6-tricarboxylic acid and 2, 6-pyridinedicarboxylic acid ligands containing N and O were used to construct cerium- and copper-based MOFs, respectively, which resulted in better charge storage and high capacitance.[27] In addition, doping of N, S and P in MOFs features a larger number of electrons/holes, causing a significant increase in conductivity.[28] 5-Sulfoisophathalic acid monosodium linkers contain phthalate groups having a high chance of binding with metals to form complexes, especially in the presence of N-donor-based co-ligands like pyridine. The hydrophilic nature of the sulfo-group facilitates hydrogen bonding to stabilize complexes. Among transition metals, copper is considered one of the most electron-rich and efficient redox-active agents.[29] Thus, the idea of utilizing SIP as well as a co-ligand such as bipyridine with copper metal to construct MOFs is very interesting for tuning the electrochemical properties of supercapacitors. Electrical conductivity in MOFs can be achieved by (1) the involvement of metal and ligand orbitals, (2) participation of π–d conjugation, (3) contribution of π–π stacking of organic ligands. 2D MOFs responsible for charge delocalization as well as π–π interaction promote layer stacking, which ultimately enhances the mobility and conductivity in the form of one-dimensional (1D) channels. The fascinating characteristics such as tunable topologies, high conductivity and porosity enable 2D MOFs to be promising candidates for excellent electrochemical energy applications.[30–33]

Although MOFs exhibit properties such as tunable pore size and high surface area but their lower conductivity may reduce their use in energy storage devices. For this purpose, conductive materials like graphene oxide (GO), reduced graphene oxide (rGO), carbon nanotubes (CNT) and MXenes have been widely used in the synthesis of MOF composites to enhance their electrochemical performance in energy storage devices, particularly in hybrid supercapacitors.[34–36] Singh *et al.* (2024) synthesized an MOF composite (MC) by integrating CNTs with Cu-MOF to enhance the conductivity of the MOF. It was found that the formation of a solid composite structure is possible by the coordination between Cu(II) of the MOF and the carboxylate groups of the CNTs. However, they also faced challenges in obtaining robust interfacial bonds and even dispersion between MOFs and CNTs, which are crucial elements for a dependable electrochemical performance. However, the results revealed a specific capacitance of 348.6 F g^{-1} at 1 A g^{-1}, energy density and power density of 27.7 W h kg^{-1} and 1640 W kg^{-1}.[37] Singh *et al.* (2021) manufactured a new Cu-based MOF composite with graphene oxide. The composite exhibits a specific capacitance of 366.6 F g^{-1} at 1 A g^{-1}. The device has an energy density of 57.2 W h kg^{-1} and power density of 4.38 kW kg^{-1}.[38] Azadfalah *et al.* (2019) combined the synergic effects of Cu-MOF with GO by synthesizing Cu-MOF/GO composites that exhibited 34.5 W h kg^{-1}, 1350 W kg^{-1} energy density and power density, respectively, at 0.5 A g^{-1}.[39] MXene is a class of 2D nitrides and carbides that is used as a conductive material for the synthesis of MOF composites. It exhibits distinct features that make it superior to other conductive materials, such as metallic conductivity, easy functionalization and hydrophilic nature.[40] In the MXene structure, the transition metal plays a vital role in the conductivity by providing conductive channels for electron transport. The other contributing factor to conductivity is the morphology of the MXene. The 2D structure of MXene facilitates in free transportation of electrons with scattering. Conductivity can also be controlled by changeable functional groups like hydroxyl (–OH) and oxygen (=O) on the terminations of MXene.[41] Thus, the incorporation of MXene can control the resistivity and conductivity of the electrode, thereby affecting the thermal stability of the battery.[42] Titanium carbide-based MXenes ($Ti_3C_2T_x$), display high conductivity because of their exceptional structural and electronic properties. The metallic conductivity owing to delocalized electrons within the 2D layers enables effective charge transport. Additionally, the functional groups (T_x) on the surface affect the conductivity because, by varying the surface terminations, the density of electronic states near the Fermi level changes, thus affecting electrical properties.[43] Hassan *et al.* (2024) explored the potential of a Zn-based MOF (MOF-5) composite with MXene (V_2CT_x), which showed a significant specific capacity of 961 C g^{-1} in three electrode assembly and 234 C g^{-1} in two electrode assembly. The hybrid assembly of MOF-5/V_2CT_x//AC, demonstrated 48.75 W h kg^{-1} as energy density and 920 W kg^{-1} as power density.[44] Hassan *et al.* (2024) also explored another Cu-BTC-based MOF composite with nitrogen-doped titanium-based MXene ($Ti_3C_2T_x$) which exhibited energy density of 65.23 W h kg^{-1} and power density of 923 W kg^{-1}. The composite showed 99% capacity retention after 8000 cycles. However, the MXene content ratio for composite preparation is very crucial for optimal results such as capacitance and cyclability. An appropriate amount of MXene in MOFs for composite synthesis prevents the re-stacking of MXene layers, which can reduce the number of electroactive sites.[45–47]

In this study, we report Cu-SIP-2D-MOFs derived from 5-sulfoisophathalic acid monosodium, 4,4-bipyridine and copper metal and their composites with MXene. Structural and morphological characterization was carried out with the help of thermogravimetric analysis (TGA), single-crystal X-ray diffraction (XRD), elemental analysis and Fourier-transform infrared (FT-IR) spectroscopy. The electrochemical performance of Cu-

SIP-MOF and its composites CM-100, CM-200 and CM-300 was also determined by cyclic voltammetry (CV), galvanostatic charge–discharge (GCD) and electrochemical impedance spectroscopy (EIS) *via* three electrode assembly, and the practical implementation of CM-200 in an asymmetric hybrid device was explored. In contrast to traditional electrode materials, the CM-200 offers significant potential for further exploration as an energy storage material. The novelty of this study revolves around the incorporation of N, S, and O (heteroatoms) in MOFs through careful selection of bi-linkers for tuning the pore size, porosity of MOFs and the integration of MXene to improve the performance of the electrode material.

2. Experimental

2.1 Materials and methods

Copper chloride dehydrate ($CuCl_2 \cdot 2H_2O$) was purchased from Alfa Acer Company, USA. 4,4-bipyridine, 5-sulfoisophthalic acid monosodium salt and MXene (Ti_3C_2) with 99.9% purity were provided by Merck Chemical Company, Germany. Distilled H_2O, ethanol, and other solvents were used as received. Overall, high analytical-grade chemicals were utilized, which are also easily accessible in the market.

2.2 Equipment

The FTIR spectrum ranged from 4000 to 400 cm^{-1}, comparing the spectra of the complex and ligand using an infrared spectrophotometer made by IR Spirit, SHIMADZU, Japan. Elementar, Vario Micro Cube elemental analyzer was employed to check the elemental % age results. Thermal analysis was conducted on TA Instrument TGA, SDT Q 600 at 10 °C min^{-1} ramp-rate. Scanning electron microscope (SEM) of Cu-SIP-MOF was performed using a JEOLJSM-6480 SEM.

2.3 Synthesis of Cu-SIP-MOF

116 mg of copper chloride dihydrate (0.68 mmol), 91 mg of SIP (0.34 mmol) and 8 mg of co-ligand, 4,4-bipyridine (0.05 mmol), were separately sonicated for 1 minute in 3 mL, 4 mL and 3 mL of distilled water, respectively. Solutions of copper chloride dihydrate and 4,4-bipyridine were added to the SIP solution. The resultant mixture was further sonicated (MSE Sanyo, Soni prep 150) for 15 minutes at a frequency of 23 kHz and an amplitude of 15 microns. The obtained solution was filtered and stored at room temperature. After 10 days, dark blue crystals appeared. Yield *ca.* 69%. Elemental analysis (%) calc. for $C_{108}H_{114}Cu_3N_{12}O_{60}S_6$ (2923.09): N, 5.75; C, 44.34; H, 3.90; S, 6.57; found: N, 5.61; C, 44.58; H, 4.12; S, 6.89. The synthesis scheme is illustrated in Fig. 1.

2.4 Fabrication of the electrode

Owing to its good conductivity, nickel foam (NF) was used as a current collector in electrochemical cells. To remove any oxide present in the NF (1.5 × 1.5 cm^2), it was washed with hydrochloric acid, ethanol and acetone, followed by drying in an oven. A normal consistency-based slurry was formed by mixing Cu-SIP-MOF (80 wt%), acetylene black (10 wt%), and polyvinylidene fluoride (10 wt%) in 50 μl of *N*-methyl-2-pyrrolidone solvent. Cu-SIP-MOF was also mixed with MXene in altered ratios of 1 : 1, 1 : 2, and 1 : 3 to prepare composites, CM-100, CM-200 and CM-300, respectively. After 12 h of thorough mixing through magnetic stirring, the MOF and its composites were deposited separately onto the nickel foam *via* the drop casting technique and dried at 60 °C for 4 h. To evaluate the performance of the best sample in the hybrid supercapacitor, an activated carbon (AC) slurry was prepared using the same material ratio and procedure. Eqn (1) was used to maintain the charge-to-mass ratio so that the maximum performance of the hybrid supercapacitor could be attained.

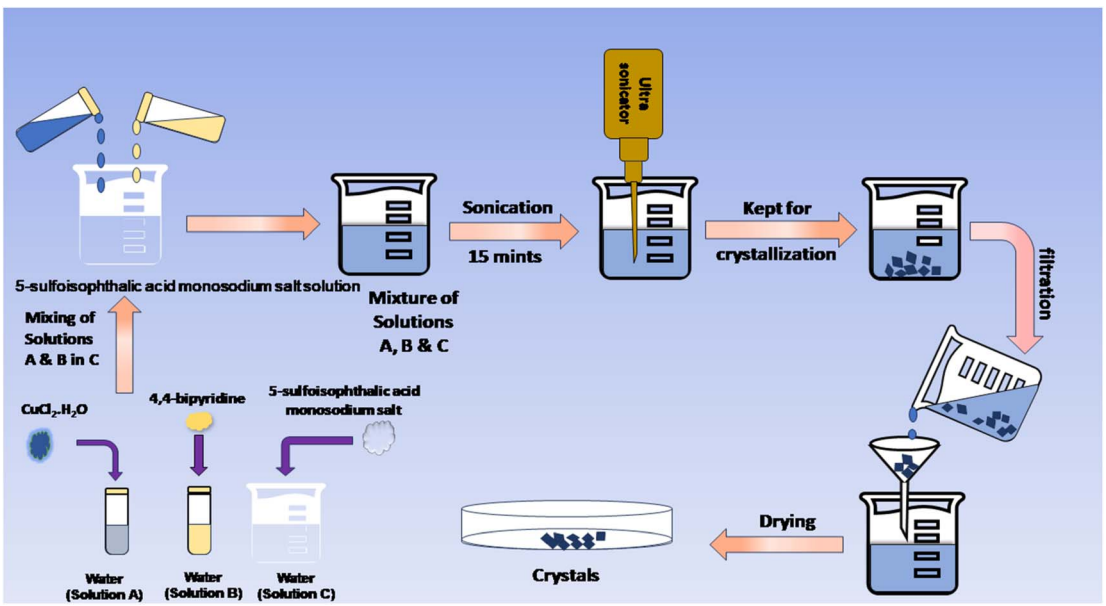

Fig. 1 Scheme for the synthesis of Cu-SIP-MOF.

$$\frac{m_+}{m_-} = \frac{C_{s-} \times \Delta V_+}{C_{s+} \times \Delta V_-} \quad (1)$$

where 'm_+' and 'm_-' are the active material masses on both electrodes. 'C_{s+}' and 'C_{s-}' represent the specific capacities on the electrode, whereas 'ΔV_+' and 'ΔV_-' are the operating voltage window.

3. Characterization techniques

3.1 FTIR, TGA and SEM analysis

FTIR, TGA further confirmed the metal–ligand binding. SEM analysis confirmed the crystalline morphology of Cu-SIP-MOF. Details are provided in the ESI (Fig. S1–S4).†

3.2 Single crystal structure of Cu-SIP-MOF

A single-crystal X-ray analysis demonstrated that the complex Cu-SIP-2D-MOF is a 2D coordination polymer. The asymmetric unit of the complex Cu-SIP-2D-MOF consists of one half and one full Cu(II) ions, two full and two half 4,4-bipyridineligands, three 5-sulfoisophthalic acid ligands and nine water molecules (Fig. 2(A)). The Cu1 atom is coordinated by four nitrogen atoms [Cu1–N bond lengths ranged between 2.009(2)–0.046(2) Å] from 4,4-bipyridine ligands and two oxygen atoms [Cu1–O1 = 2.505(2) Å and Cu1–O8 = 2.687(2) Å] from 5-sulfoisophthalic acid ligands, giving an octahedral coordination geometry, while the Cu2 atom is coordinated by four nitrogen atoms[Cu1–N3 = 2.041(2) Å, Cu1–N4 = 2.000(3) Å and Cu1–N5^{iv} = 2.014(3) Å] from 4,4-bipyridine ligands, giving a square planar coordination geometry [(iv) $x, y+1, z$]. The Cu(II) ions were bridged by 4,4-bipyridine ligands to form rectangular $[Cu_4(bpy)_4]$ clusters, with the Cu···Cu separations are 11.065 and 11.180 Å. The combination of $[Cu_4(bpy)_4]$ clusters produces a 2-D coordination polymer moving parallel to the *bc* plane (Fig. 2 (B)). Adjacent 2D coordination polymers were then connected by O–H···O, O–H···S and C–H···O hydrogen bonds (Table S3†), generating

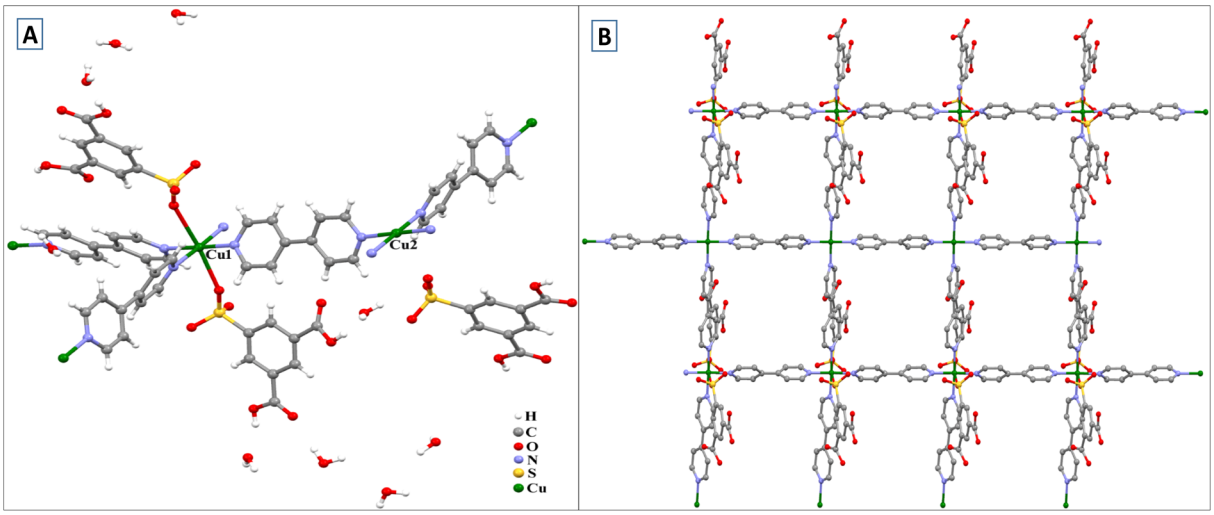

Fig. 2 (A) Molecular structure of Cu-SIP-MOF. (B) Ball and stick overview of an infinite 2D coordination polymer in Cu-SIP-MOF.

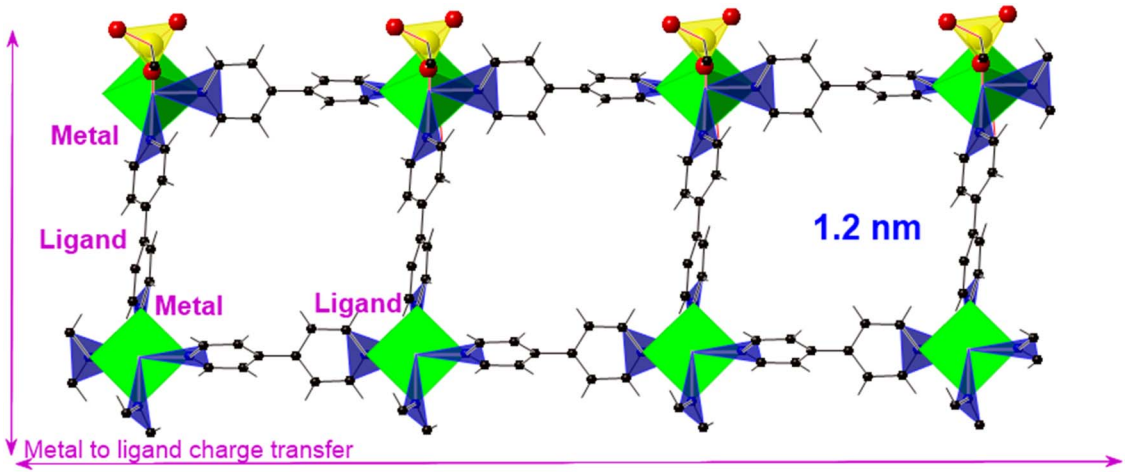

Fig. 3 Infinite polyhedral view of 2D MOF grown along the 100-direction showing cubic-shaped pores and a schematic view of the charge transport pathway through metal-to-ligand bonds.

a 3D supramolecular network (Fig. S5†). The simulated powder XRD diffractogram is shown in Fig. S6.† The improved electron delocalization in 2D MOFs is attributed to the combination of metal node d orbitals and conjugated π-orbitals of the ligand.[32,33] A polyhedral view of a 2D MOF along the 100-direction showing cubic-shaped pores of 1.2 nm and metal-to-ligand charge transfer in the 2D MOF is presented in Fig. 3.

4. Results and discussion

4.1 Half-cell electrochemical study

For the electrochemical study, an Origalys electrochemical workstation (including OrigaFlex-OGFO1A and OrigaFlex-OGFEIS) was used.

4.1.1 Cyclic voltammetry. To evaluate the electrochemical performance of Cu-SIP-MOF, CM-100, CM-200 and CM-300, 1 M KOH electrolyte was used. For the three-electrode systems, CV was conducted using silver/silver chloride as the reference and a platinum wire as the counter electrode. The cyclic voltammograms of the Cu-SIP-MOF, CM-100, CM-200 and CM-300 are shown in Fig. 4(A) to (D) with scan rates between 5 and 80 mV s^{-1} in the potential window of 0–700 mV. The comparison of Cu-SIP-MOFs and their composites at 10 mV s^{-1} showed that CM-200 had the highest area of charge storage, as shown in Fig. 4(E). As the scan rate changes, the positive and negative current values also change linearly, representing the occurrence of redox processes. Moreover, the R^2 value came close to 1, which also confirmed the reversible nature of the electrode material. Furthermore, the *b*-value (eqn (S2) and (S3)†) was also calculated to determine the nature of the material. A *b*-value within the range of 0 to 0.5 signifies battery-like material. On the other hand, a *b*-value close to 1 corresponds to capacitive domination in the material. A graph plotted between the log of anodic peak current and the log of scan rate provided the *b*-

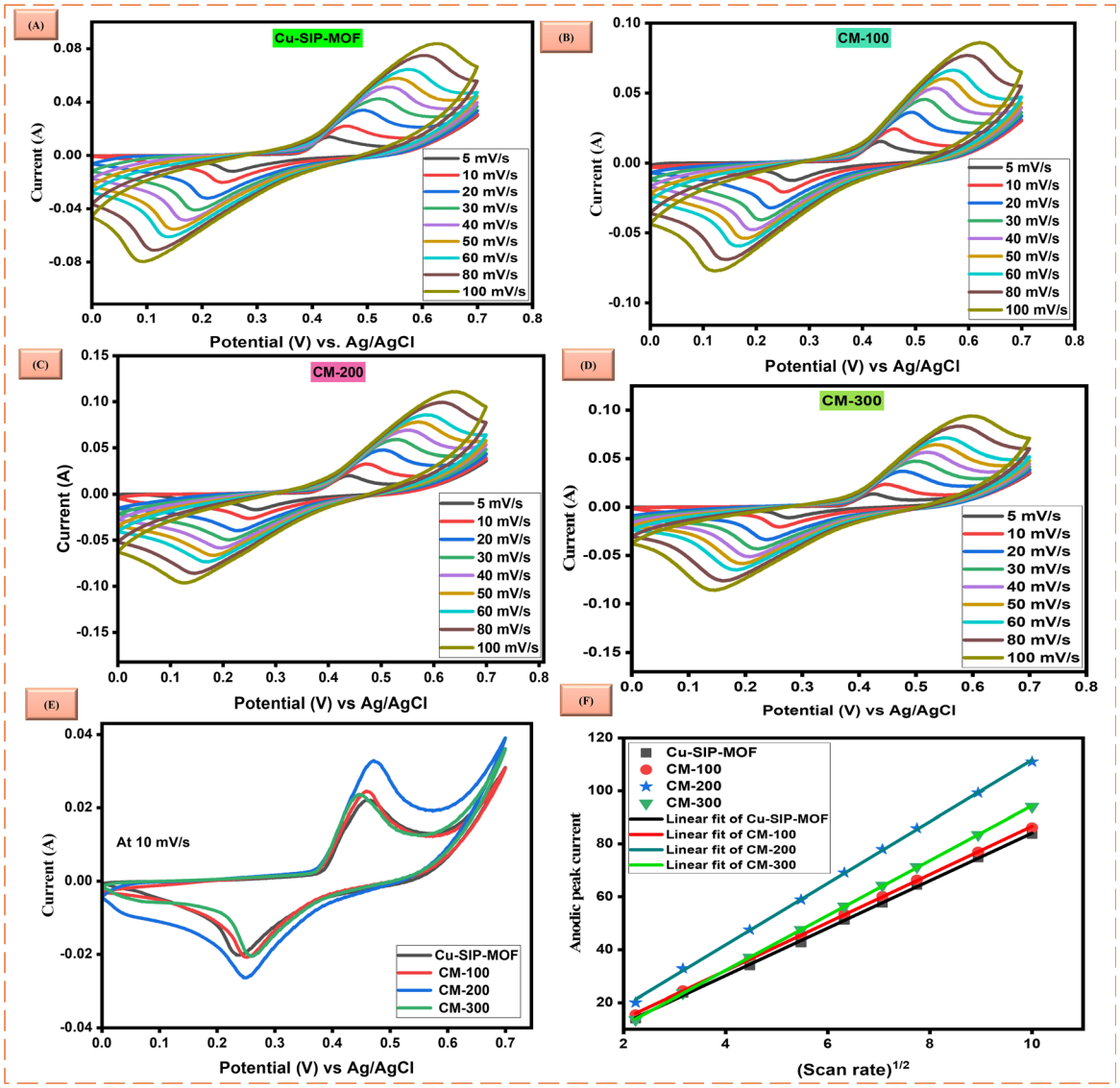

Fig. 4 (A) CV profiles of Cu-SIP-MOF, (B) CM-100, (C) CM-200 and (D) CM-300. (E) Graph of CV comparison for Cu-SIP-MOF, CM-100, CM-200 and CM-300 at 10 mV s^{-1}. (F) Plot between the square root of the scan rate and the peak current for Cu-SIP-MOF, CM-100, CM-200 and CM-300.

value for Cu-SIP-MOF, CM-100, CM-300 and CM-200, as shown in Fig. S7(A) to (D).† Cu-SIP-MOF and CM-100 demonstrated a *b*-value of 0.47, while the *b*-value for CM-300 was 0.63. CM-200 revealed a *b*-value of 0.42, which expressed that the CM-200 composite is a battery-grade predominance material. Using eqn (S5),† specific capacity for Cu-SIP-MOF, CM-100, CM-200 and CM-300 were also calculated through CV, which were 365, 392, 519 and 399 C g^{-1}, respectively, as shown in Fig. 5(A). The capacitive/diffusive contribution was also evaluated using Dunn's method (eqn (S4)†) at different scan rates. In Fig. S8(A),† the Cu-SIP-MOF capacitive and diffusive contributions are displayed as a bar graph, comparable to those of CM-100 and CM-300 in Fig. S8(D) and (G).† In comparison with the Cu-SIP-MOF and CM-300, the CM-100 exhibited higher diffusive contributions than the capacitive ones. The CM-200 column plot in Fig. 5(D) primarily shows the diffusive contributions. The faradaic/non-faradic and overall current contributions vary in the CV curves of Cu-SIP-MOF, CM-100, CM-300 and CM-200, as represented in Fig. S8(B), (E), (H),† and 5(F) at 10 mV s^{-1} and in Fig. S8(C), (F), (I)† and 5(E) at 80 mV s^{-1}. The results expressed diffusive predominance of CM-200 compared with the original MOF and other composites.

4.1.2 Galvanostatic charge–discharge (GCD). The GCD provides information about the charge storage and power capacity of the energy storage device. Plateaus in GCD represent redox reactions. The Cu-SIP-MOF, CM-100, CM-200 and CM-300

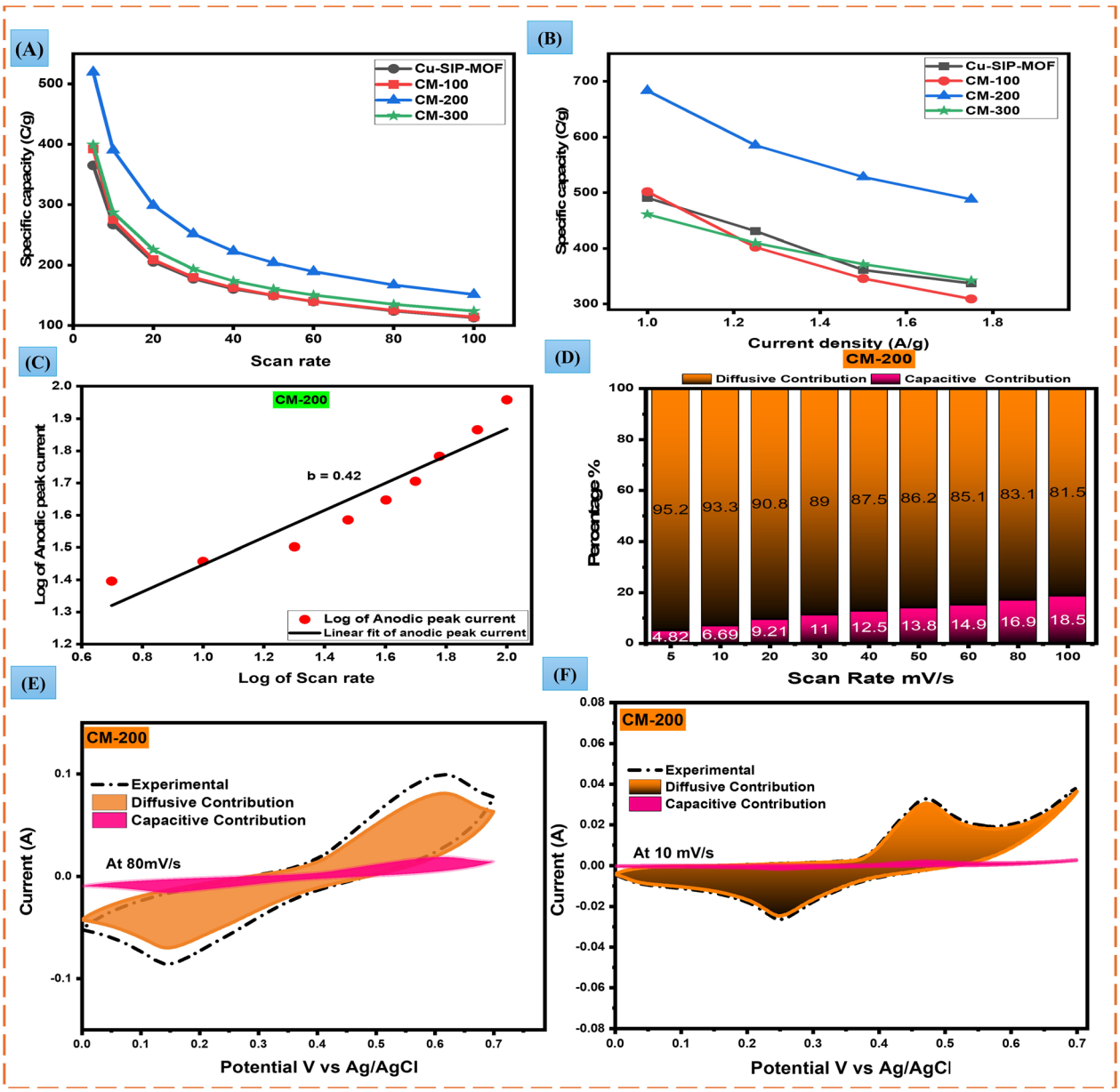

Fig. 5 (A) Specific capacities through CV at different scan rates. (B) Specific capacities calculated *via* GCD at various current densities. (C) Graph for *b*-value of CM-200. (D) Bar chart for capacitive and diffusive contributions. (E) Diffusive and capacitive contribution of CM-200 at 80 mV s^{-1}. (F) Diffusive and capacitive contribution of CM-200 at 10 mV s^{-1}.

were evaluated through charging–discharging at different current densities varying from 1 to 1.75 A g^{-1} (Fig. 5(A) to (D)). MOF and all its composites showed an increase in voltage during charging, giving a non-linear region (plateaus), which was observed upon reversing the current. Thus, the results were in coherence with the CV measurements, as CM-200 showed predominantly battery-like properties, as assessed by the graph profile and discharging time at several current densities. The

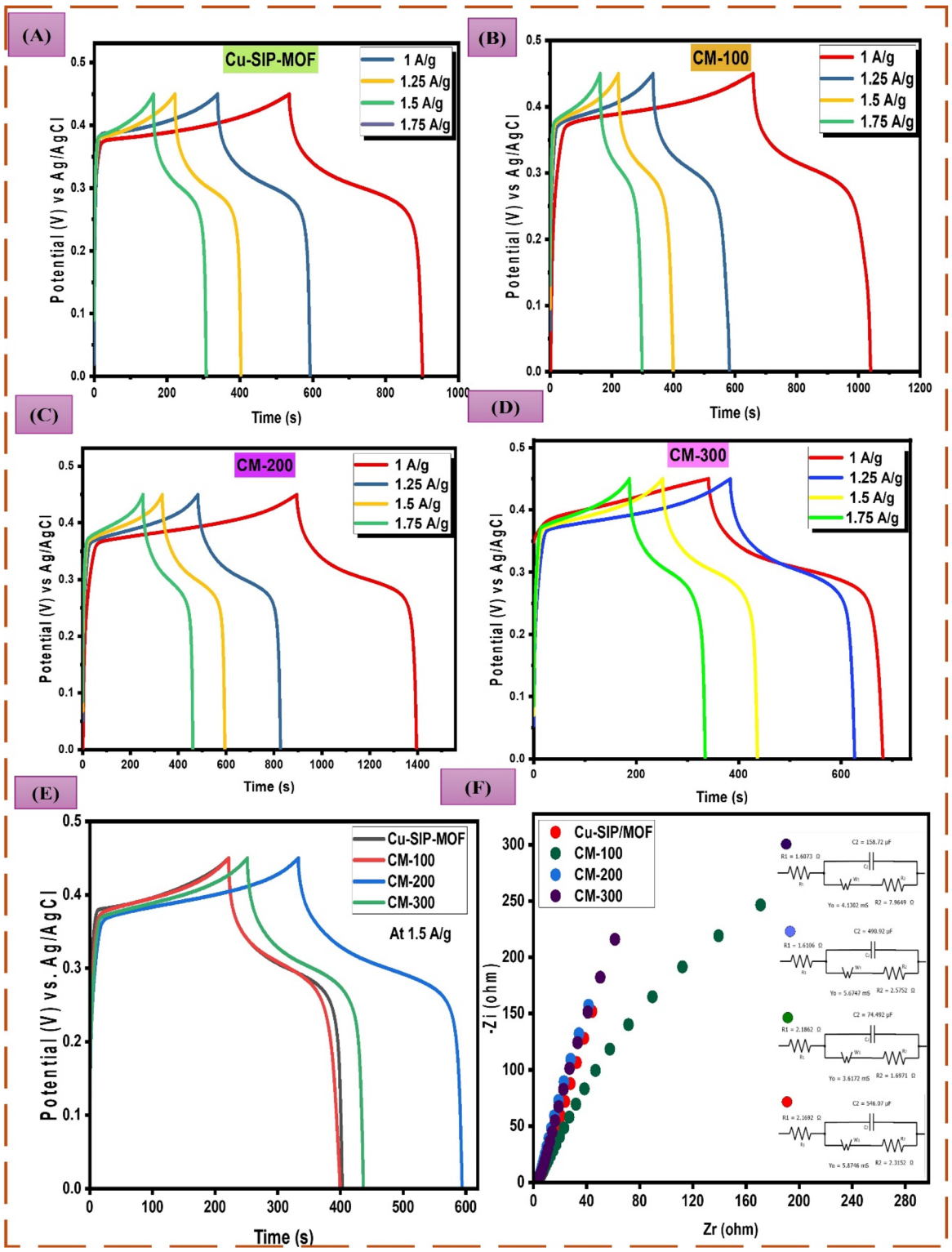

Fig. 6 (A) Galvanostatic charging–discharging at different scan rates for Cu-SIP-MOF, (B) CM-100, (C) CM-200 and (D) CM-300. (E) Comparison of GCD profiles of 1.5 A g^{-1}. (F), EIS spectra of Cu–SIP-MOF, CM-100, CM-200 and CM-300 electrodes in three-electrode systems.

specific capacity of the electrode material was determined at different current densities. Analysis through 3-electrode system revealed maximum specific capacity (eqn (S7)†) of 490.7, 501.6, 683.6 and 461 C g^{-1} for Cu-SIP-MOF, CM-100, CM-200 and CM-300, respectively, as shown in Fig. 5(B). The specific capacitances (eqn (S8)†) of Cu-SIP-MOF, CM-100, CM-200 and CM-300 were 1090.4, 1114.7, 1519.3 and 1024 F g^{-1}, respectively, as represented in Fig. S7(D).† The results show that the CM-200 is leading toward the highest energy storage consequences. Integrating MXene ($Ti_3C_2T_x$) resulted in H-bonding with the functional groups of the linker in the Cu-SIP-MOF, forming a porous composite for easy transportation of electrolyte ions and hence improving conductivity. On the other hand, the optimal balance between MOF and MXene is very important for supercapacitor applications, as excessive MXene leads to restacking due to van der Waals interactions, inhibiting ion transportation corresponding to a less accessible surface area.[48] Therefore, a lesser MXene in CM-200 provided an optimal conductive network for effective transportation of electrons. The higher MXene content in the case of CM-300 disturbed the conductive network through agglomeration, ultimately decreasing the overall performance. The significance of optimizing the MXene in MOF improve structural features and supercapacitive performance.[49]

4.1.3 Electrochemical impedance spectroscopy (EIS). EIS was performed to explain the conductivity of Cu-SIP-MOF, CM-100, CM-200 and CM-300 in the 0.1–100 kHz frequency range. The Nyquist plot between the original part of the impedance (Z_r) and imaginary part of the impedance (Z_i) yields an EIS graph with equivalent circuit fitting for Cu-SIP-MOF, CM-100, CM-200 and CM-300, Fig. 6(F). The equivalent series resistance (E_{SR}) is related to the resistance of the ions when diffusing through the

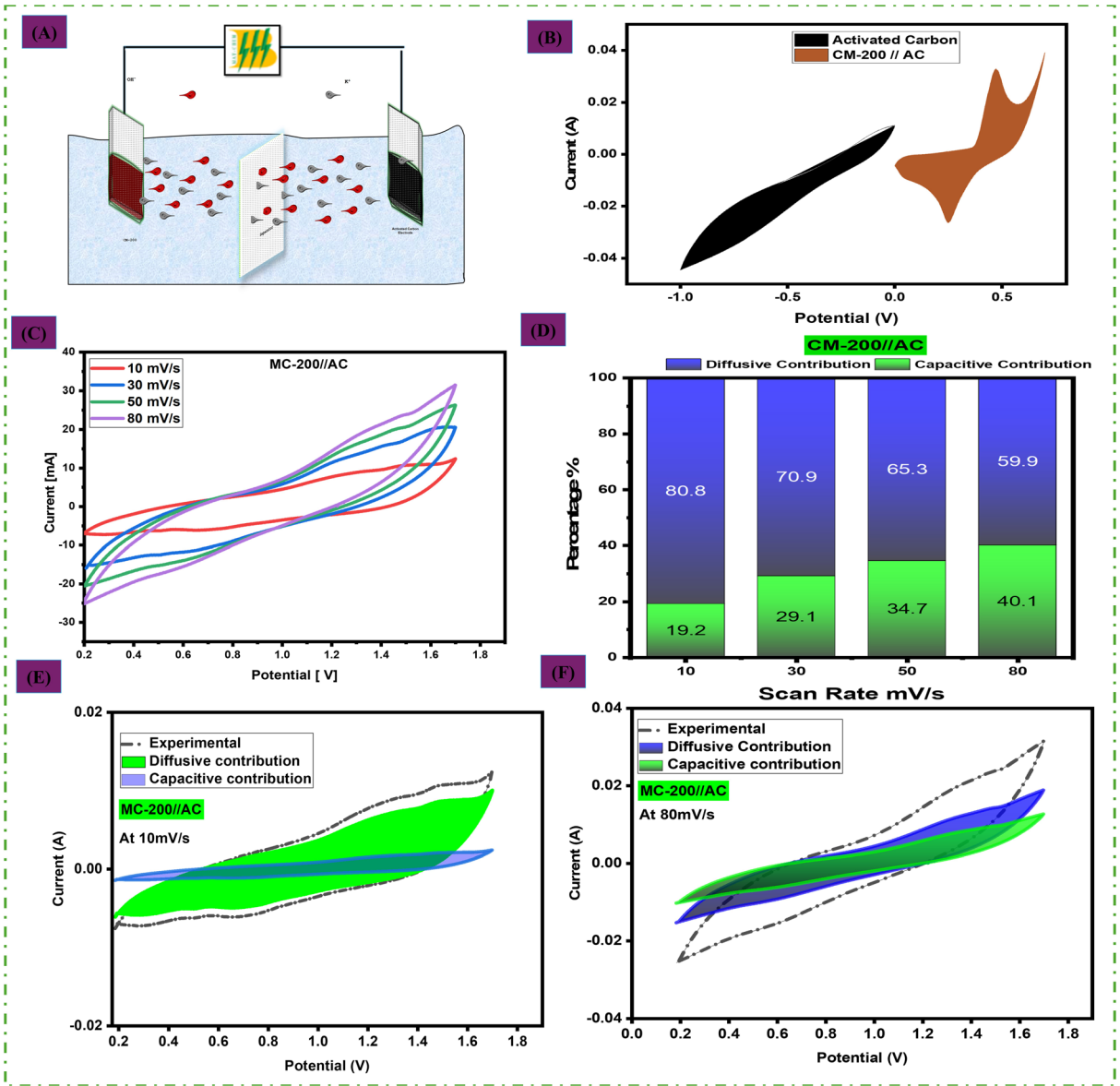

Fig. 7 (A) CM-200//AC hybrid device. (B) CV curves of CM-200 along with AC. (C) CV curves of hybrid device CM-200//AC. (D) Bar chart for capacitive and diffusive contributions. (E) Diffusive and capacitive participation at 10 mV s^{-1}. (F) Diffusive/capacitive contribution at 80 mV s^{-1}.

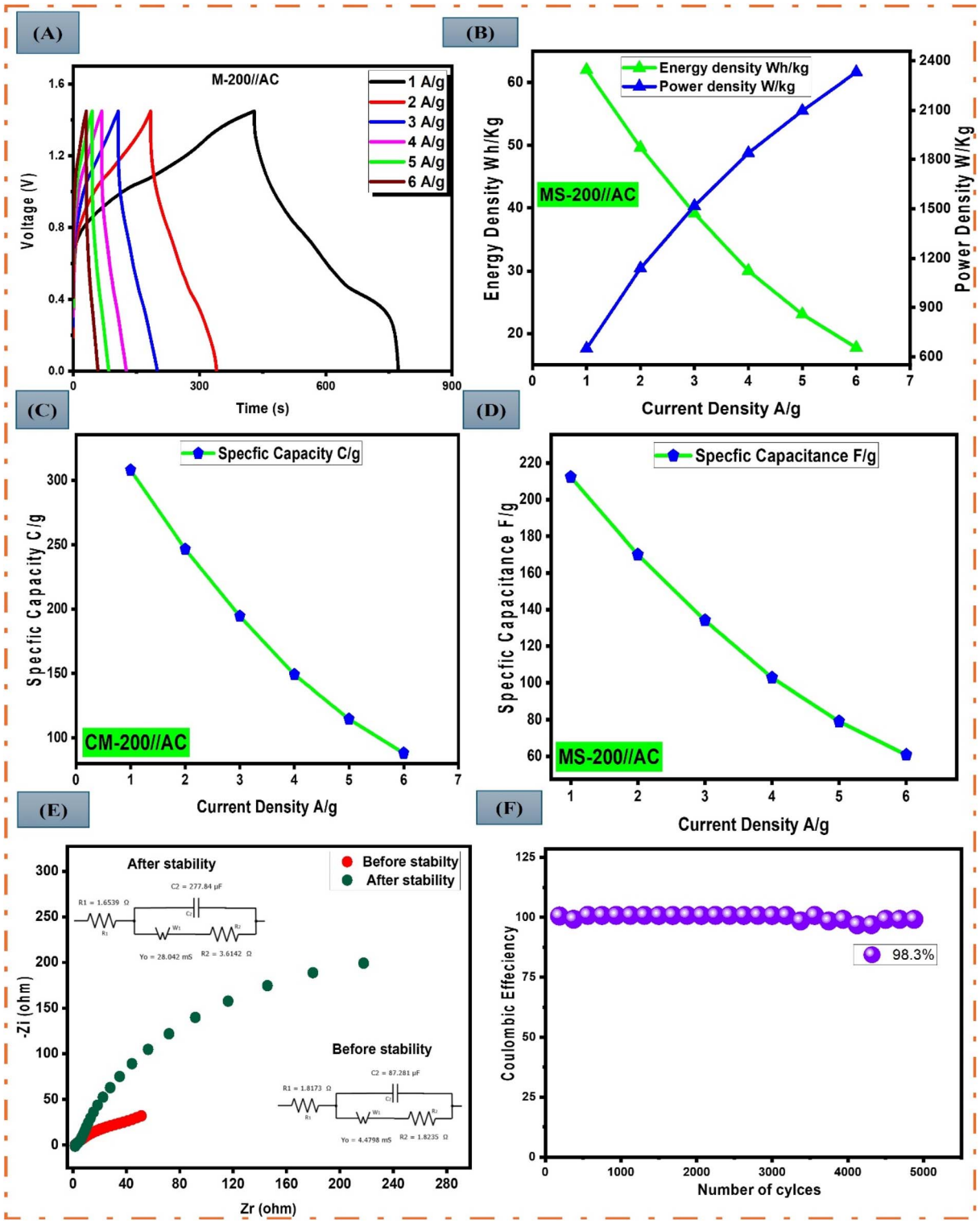

Fig. 8 (A) GCD profile at various current densities for the hybrid device. (B) Graph of energy and power density at various current densities. (C) Specific capacity for the CM-200//AC hybrid system at different current densities. (D) Specific capacitance for the CM-200//AC hybrid system at different current densities. (E) EIS spectra of CM-200//AC. (F) Plot representing coulombic efficiency after 5000 GCD cycles for the hybrid device.

electrolyte. The other type of resistance is "Interface resistance," which is ascribed to electrode electronic resistance. In the high-frequency region of the Nyquist plot, the semicircle diameter represents the charge transfer resistance (R_{ct}). The smaller the semicircle, the lower the charge transfer resistance and the higher the conductivity. The straight line corresponds to the

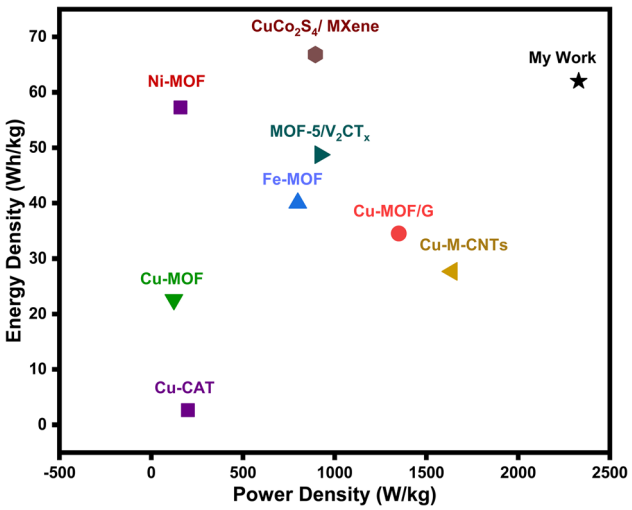

Fig. 9 Comparison of the MOF synthesized in this study with other MOFs using the Ragone plot.

Warburg impedance (Z_w), which indicates the mass transfer resistance. The E_{SR} values in the case of Cu-SIP-MOF and CM-100 were 2.1 Ω, but ESR for CM-200 and CM-300 were 1.6 Ω, revealing the lower ohmic and contact resistance of the CM-200 and CM-300. Similarly, the large diameter of the semicircle for CM-300 presented the highest R_{ct} value of 7.9 Ω while Cu-SIP-MOF, CM-100 and CM-200 showed R_{ct} values of 2.5, 1.6 and 2.3 Ω, respectively. The Warburg resistance also revealed that the CG-200 exhibited positive consequences, as the Warburg resistance value of CM-200 reflects a synergic balance between conductivity and ion accessibility. This balance appears optimal in CM-200 due to the ideal distribution of MXene and Cu-SIP MOF in the CM-200 composition, facilitating sufficient ion diffusion while maintaining structural integrity and surface redox activity.

4.2 Hybrid supercapacitor assembly

To understand the practicability of CM-200 for battery–supercapacitors hybrid, a device was constructed using activated carbon (CM-200//AC) in 1 M KOH as the electrolyte, as shown in Fig. 7(A). The electrochemical testing was performed, and Fig. 7(B) shows a CV comparison for AC and CM-200 in a two-electrode assembly.

CV was performed at various scan rates (10, 30, 50 and 80 mV s^{-1}) by adjusting a potential window of 0–1.7 V. Results depicted both pseudo-capacitive and EDLC phenomenon exhibited in the asymmetric device, as shown in Fig. 7(C). The value of the regression parameter was 0.99, which confirmed the reversibility of the current to scan rate in the device (Fig. S9(A)†). The *b*-value of 0.62 for the anodic peak (Fig. S9(B)†) also indicates capacitive-predominance in the device. Dunn's method also confirmed the pseudocapacitive predominance because of the higher capacitive contribution of the current. Fig. 7(D) illustrates the continuous increase in capacitive contribution with increasing scan rate. At 10 and 80 mV s^{-1} scan rates, the diffusion and capacitive contributions of current are shown for the experimental value in Fig. 7(E) and (F). An increase in the capacitive contribution is attributed to the occurrence of the EDLC phenomenon at higher scan rates, as less time is required for the ions to intercalate.

GCD was performed at various current densities (1–6 Ag^{-1}) with a potential window of 0–1.7 V (Fig. 8(A)). As the current density increased, the discharging time decreased. The CM-200//AC electrode material showed a high energy density of 62 W h kg^{-1} and a power density of 2330.4 W kg^{-1} using eqn (S9) and (S10)† are also shown in Fig. 8(B). The device demonstrated specific capacity and capacitance of 307 C g^{-1} and 212 F g^{-1}, respectively, as depicted in Fig. 8(C) and (D). Through stability tests, the hybrid material was found to exhibit high stability and efficiency. After 5000 GCD cycles, the coulombic efficiency was maintained at 98.3% (Fig. 8(F)). The conductivity of the device was assessed by EIS in the frequency range of 0.1 to 100 kHz. Through circuit fitting on the Nyquist plot, the complete circuit of the electrode was obtained. After stability, the E_{SR} value was 1.6539 Ω, whereas the value of R_{ct} came out as 3.6142 Ω. A Nyquist plot with a smaller semicircle shows low resistance for charge transfer and high conductivity. The straight line represents the Warburg impedance (Z_w), which is related to the mass transfer resistance (Fig. 8 (E)). The results of the CM-200//AC electrode are promising for electrode usage in forthcoming hybrid supercapacitors.

5. Conclusions

In summary, a new copper(II) MOF, Cu–SIP-MOF, was synthesized, characterized and evaluated for electrochemical performance with its composites with MXene (CM-100, CM-200 and CM-300). The electrochemical properties of the fabricated electrode materials were investigated through a three-electrode assembly process using CV, GCD and EIS. CM-200 was evaluated as the best sample because it exhibited a specific capacity of 683.6 C g^{-1} through GCD. Due to the significant results of CM-200, a hybrid supercapacitor assembly was constructed as CM-200//AC, which showed energy and power density of 62 W h kg^{-1} and 2330.4 W kg^{-1}, respectively. The capacitive and diffusive contributions of the current were determined by Dunn's method. This study provides a valuable perspective that using N, S, and O heteroatom-based bi-linkers, the pore size, shape and porosity of MOFs can be controlled. 2D MOF facilitates the charge transport and optimization in the ratio of conductive materials, resulting in improved characteristics for utilization in advanced battery, supercapacitor hybrid devices. A comparison of the MOF synthesized in this study with other MOFs using a Ragone plot is presented in Fig. 9 and Table S4.†

Data availability

The data supporting this article have been included as part of the ESI.†

Author contributions

Maham: writing original draft, Shahzad: supervision, Javed: characterization, Tayyaba: investigation, Muhammad: formal

analysis, Azhar: visualization, Ayesha: validation, Onur: XRD software, Sundas: methodology.

Conflicts of interest

All authors declare that there are no competing interests.

Acknowledgements

We gratefully acknowledge financial assistance from the Higher Education Commission of Pakistan, HEC-NRPU project no. 20-17612/NRPU/R&D/HEC/2021, and the Office of Research Innovation & Commercialization (ORIC), Govt. College University Lahore, Project No. 378/ORIC/24.

References

1 H. D. Yoo, E. Markevich, G. Salitra, D. Sharon and D. Aurbach, On the challenge of developing advanced technologies for electrochemical energy storage and conversion, *Mater. Today*, 2014, **17**(3), 110–121.
2 D. Larcher and J.-M. Tarascon, Towards greener and more sustainable batteries for electrical energy storage, *Nat. Chem.*, 2015, **7**(1), 19–29.
3 M. S. Javed, *et al.*, The emergence of 2D MXenes based Zn-ion batteries: recent development and prospects, *Small*, 2022, **18**(26), 2201989.
4 S. Dai, *et al.*, In situ Raman study of nickel bicarbonate for high-performance energy storage device, *Nano Energy*, 2019, **64**, 103919.
5 M. Z. Iqbal, U. Aziz, M. W. Khan, S. Siddique, M. Alzaid and S. Aftab, Strategies to enhance the electrochemical performance of strontium-based electrode materials for battery-supercapacitor applications, *J. Electroanal. Chem.*, 2022, **924**, 116868.
6 M. S. Javed, *et al.*, An ultra-high energy density flexible asymmetric supercapacitor based on hierarchical fabric decorated with 2D bimetallic oxide nanosheets and MOF-derived porous carbon polyhedra, *J. Mater. Chem. A*, 2019, **7**(3), 946–957.
7 M. Zahir Iqbal, N. Amjad and M. Waqas Khan, Metal-organic-framework as novel electrode materials for hybrid battery-supercapacitor applications, *ChemElectroChem*, 2022, **9**(17), e202200036.
8 L. Yang, *et al.*, Anthraquinone-modified nitrogen-doped graphene aerogel for boosting energy density of supercapacitors by self-matching of capacity, *Electrochim. Acta*, 2021, **393**, 139057.
9 S. Sagadevan *et al.*, Fundamental electrochemical energy storage systems, in *Advances in Supercapacitor and Supercapattery*, Elsevier, 2021, pp. 27–43.
10 M. S. Javed, H. Lei, Z. Wang, B. Liu, X. Cai and W. Mai, 2D V2O5 nanosheets as a binder-free high-energy cathode for ultrafast aqueous and flexible Zn-ion batteries, *Nano Energy*, 2020, **70**, 104573.
11 Y. Ma, *et al.*, Recent advances in transition metal oxides with different dimensions as electrodes for high-performance supercapacitors, *Adv. Compos. Hybrid Mater.*, 2021, 1–19.
12 S. Manoharan, K. Krishnamoorthy, A. Sathyaseelan and S.-J. Kim, High-power graphene supercapacitors for the effective storage of regenerative energy during the braking and deceleration process in electric vehicles, *Mater. Chem. Front.*, 2021, **5**(16), 6200–6211.
13 M. S. Javed, *et al.*, High performance solid state flexible supercapacitor based on molybdenum sulfide hierarchical nanospheres, *J. Power Sources*, 2015, **285**, 63–69.
14 M. Z. Iqbal and U. Aziz, Supercapattery: Merging of battery-supercapacitor electrodes for hybrid energy storage devices, *J. Energy Storage*, 2022, **46**, 103823.
15 W. J. Basirun, I. M. Saeed, M. S. Rahman and S. A. Mazari, Nickel oxides/hydroxides-graphene as hybrid supercapattery nanocomposites for advanced charge storage materials–a review, *Crit. Rev. Solid State Mater. Sci.*, 2021, **46**(6), 553–586.
16 E. Dhandapani, S. Thangarasu, S. Ramesh, K. Ramesh, R. Vasudevan and N. Duraisamy, Recent development and prospective of carbonaceous material, conducting polymer and their composite electrode materials for supercapacitor—A review, *J. Energy Storage*, 2022, **52**, 104937.
17 M. M. Faisal, S. R. Ali, K. C. Sanal, M. W. Iqbal, M. Z. Iqbal and A. Saeed, Highly porous terpolymer-MOF composite electrode material for high performance supercapattery devices, *J. Electroanal. Chem.*, 2021, **893**, 115321.
18 C. Liu, Y. Bai, W. Li, F. Yang, G. Zhang and H. Pang, In situ growth of three-dimensional MXene/metal–organic framework composites for high-performance supercapacitors, *Angew. Chem., Int. Ed.*, 2022, **61**(11), e202116282.
19 J. Pokharel, *et al.*, MOF-derived hierarchical carbon network as an extremely-high-performance supercapacitor electrode, *Electrochim. Acta*, 2021, **394**, 139058.
20 S. Chuhadiya, D. Suthar, S. L. Patel and M. S. Dhaka, Metal organic frameworks as hybrid porous materials for energy storage and conversion devices: A review, *Coord. Chem. Rev.*, 2021, **446**, 214115.
21 T. Chen, *et al.*, In situ synthesis of MOF-74 family for high areal energy density of aqueous nickel–zinc batteries, *Adv. Mater.*, 2022, **34**(30), 2201779.
22 X. Zhao, K. Tao and L. Han, Self-supported metal–organic framework-based nanostructures as binder-free electrodes for supercapacitors, *Nanoscale*, 2022, **14**(6), 2155–2166.
23 Q. Bi, Q. Ma, K. Tao and L. Han, Hierarchical core–shell 2D MOF nanosheet hybrid arrays for high-performance hybrid supercapacitors, *Dalton Trans.*, 2021, **50**(23), 8179–8188.
24 X. Yang, *et al.*, Tailoring ion-accessible pores of robust nitrogen heteroatomic carbon nanoparticles for high-capacity and long-life Zn-ion storage, *J. Energy Storage*, 2024, **104**, 114509.
25 J. H. Shah, *et al.*, Redox active cobalt based bi-linker metal organic frameworks derived from 5-sulfoisopthalic acid

and 4, 4-bipyridine for supercapacitor, *Mater. Res. Bull.*, 2025, **181**, 113123.
26 M. Shahbaz, S. Sharif, A. Shahzad, Z. S. Ṣahin, B. Riaz and S. Shahzad, Enhanced electrochemical performance of cerium-based metal organic frameworks derived from pyridine-2, 4, 6-tricarboxylic acid for energy storage devices, *J. Energy Storage*, 2024, **88**, 111463.
27 J. H. Shah, *et al.*, Electrochemical investigation of copper 1D conductive polymer for hybrid supercapacitor applications, *J. Energy Storage*, 2024, **102**, 114058.
28 Y. Peng, Y. Bai, C. Liu, S. Cao, Q. Kong and H. Pang, Applications of metal–organic framework-derived N, P, S doped materials in electrochemical energy conversion and storage, *Coord. Chem. Rev.*, 2022, **466**, 214602.
29 Q. Bi, Q. Ma, K. Tao and L. Han, Hierarchical core–shell 2D MOF nanosheet hybrid arrays for high-performance hybrid supercapacitors, *Dalton Trans.*, 2021, **50**(23), 8179–8188.
30 Z. Ye, Y. Jiang, L. Li, F. Wu and R. Chen, Rational design of MOF-based materials for next-generation rechargeable batteries, *Nano-Micro Lett.*, 2021, **13**, 1–37.
31 L. S. Xie, G. Skorupskii and M. Dinca, Electrically conductive metal–organic frameworks, *Chem. Rev.*, 2020, **120**(16), 8536–8580.
32 R. Li, X. Yan and L. Chen, 2D Conductive Metal–Organic Frameworks for Electrochemical Energy Application, *Org. Mater.*, 2024, **6**(02), 45–65.
33 J. Liu, G. Xing and L. Chen, 2D Conjugated Metal–Organic Frameworks: Defined Synthesis and Tailor-Made Functions, *Acc. Chem. Res.*, 2024, **57**(7), 1032–1045.
34 K. W. Nam, *et al.*, Conductive 2D metal-organic framework for high-performance cathodes in aqueous rechargeable zinc batteries, *Nat. Commun.*, 2019, **10**(1), 4948.
35 L. Guo, J. Sun, J. Wei, Y. Liu, L. Hou and C. Yuan, Conductive metal-organic frameworks: recent advances in electrochemical energy-related applications and perspectives, *Carbon Energy*, 2020, **2**(2), 203–222.
36 J. Ren, *et al.*, Twisting carbon nanotube fibers for both wire-shaped micro-supercapacitor and micro-battery, *Adv. Mater.*, 2013, **25**(8), 1155–1159.
37 M. K. Singh, S. Krishnan, K. Singh and D. K. Rai, CNT Interwoven Cu-MOF: A Synergistic Electrochemical Approach for Solid-State Supercapacitor and Hydrogen Evolution Reaction, *Energy Fuels*, 2024, **38**, 12098–12110.
38 M. K. Singh, A. K. Gupta, S. Krishnan, N. Guha, S. Marimuthu and D. K. Rai, A new hierarchically porous Cu-MOF composited with rGO as an efficient hybrid supercapacitor electrode material, *J. Energy Storage*, 2021, **43**, 103301.
39 M. Azadfalah, A. Sedghi and H. Hosseini, Synthesis of nano-flower metal–organic framework/graphene composites as a high-performance electrode material for supercapacitors, *J. Electron. Mater.*, 2019, **48**(11), 7011–7024.
40 M. Safarkhani, *et al.*, Engineering MXene@ MOF composites for a wide range of applications: a perspective, *ACS Appl. Eng. Mater.*, 2023, **1**(11), 3080–3098.
41 M. Sun, W. Ye, J. Zhang and K. Zheng, Structure, Properties, and Preparation of MXene and the Application of Its Composites in Supercapacitors, *Inorganics*, 2024, **12**(4), 112.
42 J. L. Hart, *et al.*, Control of MXenes' electronic properties through termination and intercalation, *Nat. Commun.*, 2019, **10**(1), 522.
43 N. Boussadoune, O. Nadeau and G. Antonius, Electronic transport in titanium carbide MXenes from first principles, *Phys. Rev. B*, 2023, **108**(12), 125124.
44 H. Hassan, *et al.*, Innovative MOF-5/V2CTx composite for high-performance, and ultra-fast supercapacitors and hydrogen evolution reaction, *Electrochim. Acta*, 2024, **489**, 144277.
45 H. Hassan, *et al.*, Effect of electrolyte optimization on nitrogen-doped MXene (Ti 3 C 2 T x) coupled with Cu–BTC MOF for a supercapattery and the hydrogen evolution reaction, *New J. Chem.*, 2024, **48**(14), 6277–6295.
46 D. Xu, Z. Zhang, K. Tao and L. Han, A heterostructure of a 2D bimetallic metal–organic framework assembled on an MXene for high-performance supercapacitors, *Dalton Trans.*, 2023, **52**(8), 2455–2462.
47 X. Chen, Z. Ding, H. Yu, H. Ge, W. Liu and S. Sun, Facile fabrication of CuCo 2 S 4 nanoparticles/MXene composite as anode for high-performance asymmetric supercapacitor, *Mater. Chem. Front.*, 2021, **5**(20), 7606–7616.
48 B. M. Omkaramurthy, G. Krishnamurthy and S. Foro, Synthesis and characterization of mesoporous crystalline copper metal–organic frameworks for electrochemical energy storage application, *SN Appl. Sci.*, 2020, **2**(3), 342.
49 R. Zhu, Y. Gu, L. Liu, J. Lu and H. Pang, Integration of conductive MOF and MXene for high-performance supercapacitor, *New J. Chem.*, 2024, **48**(23), 10593–10598.